Deep Resources Engineering 2 (2025) 100170

Contents lists available at ScienceDirect

Deep Resources Engineering

journal homepage: www.keaipublishing.com/en/journals/deepre/

Three-dimensional deformation response of cement stone under true triaxial compression

Ying Xu [a], Dongping Liu [a], Bangbiao Wu [a,b], Jiacun Liu [a,*]

[a] State Key Laboratory of Hydraulic Engineering Intelligent Construction and Operation, Tianjin University, Tianjin 300072, China
[b] Department of geotechnical engineering, University of Kassel, Kassel 34125, Germany

ARTICLE INFO

Keywords:
Cement stone
True triaxial stress
Intermediate principal stress
Principal strain space
Lode angle dependence

ABSTRACT

Three-dimensional deformation properties of cement stone are crucial for the stability and safety of shafts. To explore these properties, a series of true triaxial tests adopting common loading path (constant intermediate principal stress and minimum principal stress) were performed on the cement stone samples. The relationship between principal strains was examined. To investigate the correlation between shear and volumetric strains, the strain paths within meridian plane are analyzed. Under low intermediate principal stress, the volumetric strain tends to develop with increasing intermediate principal stress. Conversely, under high intermediate principal stress, the shear strain tends to develop with increasing intermediate principal stress. To examine the Lode angle dependence of deformation, the concept of the deflection Lode angle under common loading path is first introduced. The strain paths within the deviatoric plane are then analyzed. The deflection Lode angle is negatively correlated with the intermediate principal stress. With increasing intermediate principal stress, the deflection Lode angle transitions from positive to negative. Furthermore, the Lode dependence of deformation decreases significantly as the minimum principal stress increases.

1. Introduction

With the increasing exploitation of underground resources and space, underground engineering is gradually extending deeper into the Earth's crust [1–3]. Shafts play a crucial role in oil and gas exploration, carbon dioxide sequestration, and geothermal extraction [4–6]. To ensure the stability and safety of these shafts, cement stone is widely used to seal the gap between the formation and the casing [7,8]. Furthermore, under the combined effect of geostress and engineering disturbances, the cement stone is subjected to true triaxial stress states [9]. Therefore, it is crucial to investigate the three-dimensional (3D) deformation response of cement stone under such a stress condition.

The true triaxial stress state is categorized as a 3D stress state, emphasizing the effect of the intermediate principal stress (σ_2) on geotechnical materials [1]. This stress state primarily influences properties such as strength property [9–13], stress-strain relationship [14,15], and failure modes [15,16]. With increasing σ_2, the strength of geotechnical material generally follows a trend of first increasing and then decreasing [1,17–20]. Under the influence of σ_2, the stress-strain behavior of geotechnical material exhibits anisotropy [16], particularly in the intermediate principal strain. With increasing σ_2, the intermediate principal strain transitions from dilation to contraction [21–24]. However, different geotechnical materials exhibit distinct variations in failure modes. The brittleness of Coconino sandstone and Bentheim sandstone increases with increasing σ_2 [17], whereas the ductility of coal increases with increasing σ_2 [25,26]. In summary, the mechanical response of geotechnical materials under true triaxial stress states demonstrates non-monotonicity and anisotropy.

The deformation response, strength properties, and failure modes of geotechnical materials have been extensively studied [27]. In particular, the deformation response of geotechnical materials has primarily been analyzed through the stress-strain curve, focusing on the correlation between stress and strain. However, the stress-strain curve alone cannot adequately capture the strain-to-strain relationship [16]. Therefore, a more comprehensive analysis of the 3D deformation response is necessary, based on the 3D principal strain space [16]. Despite its importance, the deformation response of geotechnical materials within the 3D principal strain space has not received significant attention from scholars. Only a few studies have addressed the 3D deformation response of geotechnical materials within the 3D principal strain space, including cement stone [16], Vosges sandstone [28], and Chayuan sandstone [29]. Specifically, the three-dimensional strain path of

* Corresponding author.
E-mail address: jiacun1024@163.com (J. Liu).

https://doi.org/10.1016/j.deepre.2025.100170
Received 17 December 2024; Received in revised form 28 February 2025; Accepted 9 March 2025
Available online 13 March 2025

cement stone under a constant Lode angle loading path is analyzed [16], including the principal strain space, deviatoric plane, and meridian plane. The relationship between shear strain and volumetric strain in Vosges sandstone under a constant Lode angle and hydrostatic pressure loading path is examined [28]. The deformation characteristics within the deviatoric plane of Chayuan sandstone under a constant Lode angle and hydrostatic pressure loading path is analyzed [29]. Among these three-dimensional deformation characteristics of geotechnical materials, it is noteworthy that both experimental result and theoretical analysis indicate that the deformation response of geotechnical materials exhibits Lode angle dependence (LAD) [16,29–31], which can be directly observed through the strain path within the deviatoric plane. The LAD is crucial for accurately describing the deformation of geotechnical materials [14,30,31]. However, the relationship between LAD and intermediate principal stress remains unclear, and further investigation into the deformation response of geotechnical materials within the 3D principal strain space is needed.

In this study, the experimental methodology is first presented. Then, the geometric presentation of strain and stress state and concept of Lode dependence of deformation is introduced. Building on these concepts, the strains paths within 3D principal strain space are discussed.

2. Experimental program

In this study, the cement stone was adopted to conduct a series of true triaxial tests. The formulation of the cement stone is consistent with that described in our previous research [9]. The primary components of cement stone are calcium silicate hydrate and portlandite. Detailed scanning electron microscopy and X-ray diffraction analyses of cement stone sample can be found in our previous studies [9,16,24]. The cement stone samples were ground to standard 100 mm × 100 mm × 100 mm cube, as depicted in Fig. 1c. Additionally, the non-uniformity and non-perpendicularity of cement stone sample were maintained below 0.02 mm.

The true triaxial system adopted in this study is from Tianjin University [9], as shown in Fig. 1a. The true triaxial testing system consists of a data acquisition system, a true triaxial pressure cell, and a servo-controlled loading system. This system is capable of applying a maximum load of 4000 kN in the X and Y directions, and 2700 kN in the Z direction. Additionally, the true triaxial testing system employs a fully symmetrical design to prevent displacement of the sample's center during both the loading and unloading phases. Two linear variable displacement transducers (LVDTs) are positioned in each principal stress direction to measure the strain of cement stone, as depicted in Fig. 1a. Based on the suggested method of International Society for Rock Mechanics and Rock Engineering (ISRM) [32], the common loading path shown in Fig. 1b is adopted in this study. The adopted loading path consists of three stages: (1) the cement stone sample is subjected to hydrostatic pressure with a loading rate of 0.2 MPa/s. (2) the minimum principal stress (σ_3) is kept constant at a preset value. The maximum principal stress (σ_1) and intermediate principal stress (σ_2) are remained equal and increase at a loading rate of 0.2 MPa/s. At this stage, the cement stone is under the triaxial extension state. (3) σ_3 and σ_2 remains constant at a preset value, while σ_1 continues to increase at a loading rate of 0.1 MPa/s until the peak strength of cement stone is reached. At this point, the cement stone is subjected to a true triaxial stress state. The specific test conditions for the common loading path is illustrated in Table 1. This study aims to investigate the 3D deformation response of cement stone within the 3D principal strain space. Consequently, the detailed stress-strain curves for cement stone are provided in the

Table 1
Test condition of loading path.

σ_3/MPa	σ_2/MPa
5	5/20/30/45
10	10/20/30/45/60
20	20/40/60/80

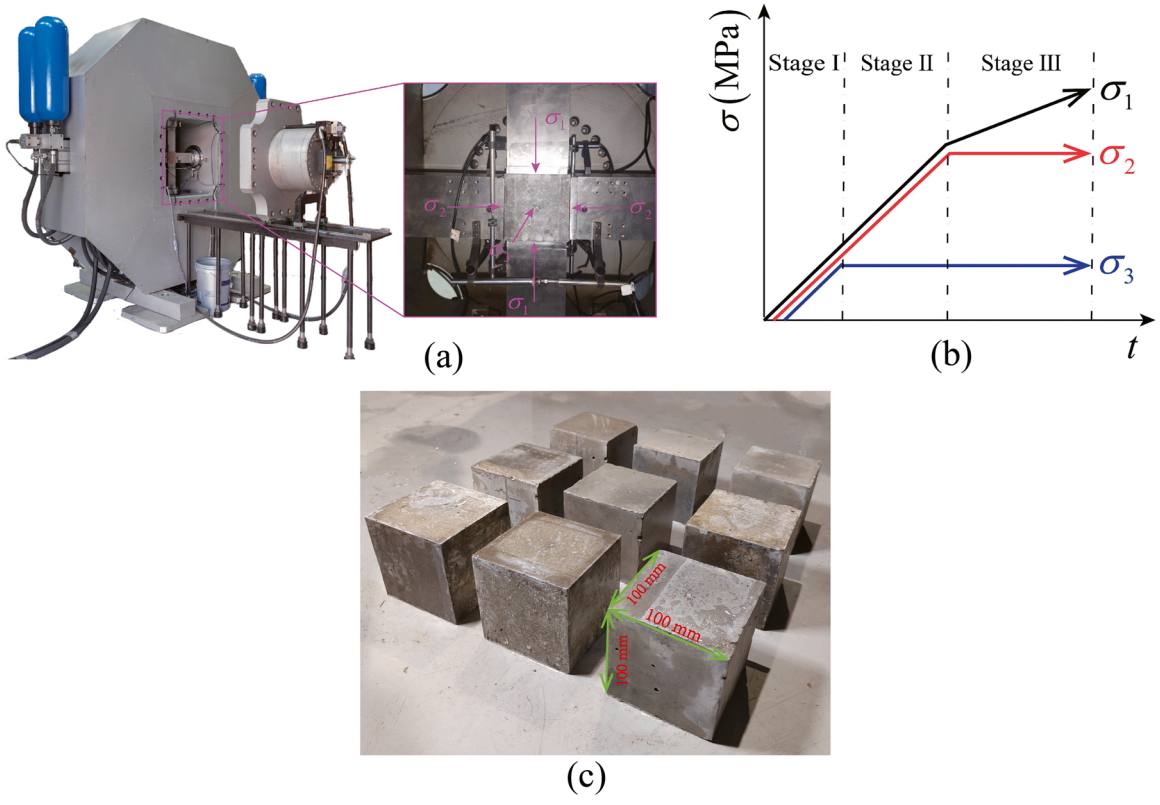

Fig. 1. Experimental methodology. (a) True triaxial testing system; (b) Loading path; (c) Cement stone sample.

Appendix.

3. Preliminary information

3.1. Geometric presentation of strain and stress states

Before examining the 3D deformation response of cement stone, it is essential to first introduce the concepts of principal strain and stress spaces. Any strain state within the principal strain space can be identified by $(\varepsilon_1,\varepsilon_2,\varepsilon_3)$, as shown in Fig. 2a. Besides, any stress state within the principal stress space can be identified by $(\sigma_1,\sigma_2,\sigma_3)$, as shown in Fig. 2b. The hydrostatic axis with the same principal strain and stress is in the direction of OO'. The plane incorporating the axis OO' is known as meridian plane [16]. The plane vertical to the meridian plane is known as deviatoric plane [16]. For strain state, the strain can be decomposed into shear strain and volumetric strain. The invariant ξ_ε is the length of OO', reflecting the extent of volumetric deformation. The invariant r_ε is the length of $A_\varepsilon O'$, reflecting the extent of shear deformation. The Lode angle for strain θ_ε is known as the angle from the perpendicular line of ε'_2 axis to $A_\varepsilon O'$, as shown in Fig. 2a. θ_ε is equal to -30° under triaxial compression state ($\varepsilon_2 = \varepsilon_3$). θ_ε is equal to 30° under triaxial extension state ($\varepsilon_1 = \varepsilon_2$). Therefore, the strain state within the 3D principal strain space can be also identified by $(\xi_\varepsilon,r_\varepsilon,\theta_\varepsilon)$, given by [16]:

$$\left.\begin{aligned} \xi_\varepsilon &= \frac{I'_1}{\sqrt{3}} \\ r_\varepsilon &= \sqrt{2J'_2} \\ \theta_\varepsilon &= \frac{1}{3}\sin^{-1}\left(-\frac{3\sqrt{3}}{2}\frac{J'_3}{J'^{3/2}_2}\right) \end{aligned}\right\} \tag{1}$$

with

$$\left.\begin{aligned} I'_1 &= \varepsilon_1+\varepsilon_2+\varepsilon_3 \\ I'_2 &= \varepsilon_1\varepsilon_2+\varepsilon_1\varepsilon_3+\varepsilon_2\varepsilon_3 \\ I'_3 &= \varepsilon_1\varepsilon_2\varepsilon_3 \\ J'_2 &= \frac{[(\varepsilon_1-\varepsilon_2)^2+(\varepsilon_1-\varepsilon_3)^2+(\varepsilon_2-\varepsilon_3)^2]}{6} \\ J'_3 &= \frac{2I'^3_1-9I'_1I'_2+27I'_3}{27} \end{aligned}\right\} \tag{2}$$

where ε_1 is maximum principal strain; ε_2 is intermediate principal strain; ε_3 is minimum principal strain, I'_1 is the first invariant of the strain tensor, I'_2 is the second invariant of the strain tensor, I'_3 is the third invariant of the strain tensor, J'_2 is the second invariant of the deviatoric strain tensor, J'_3 is the third invariant of the deviatoric strain tensor.

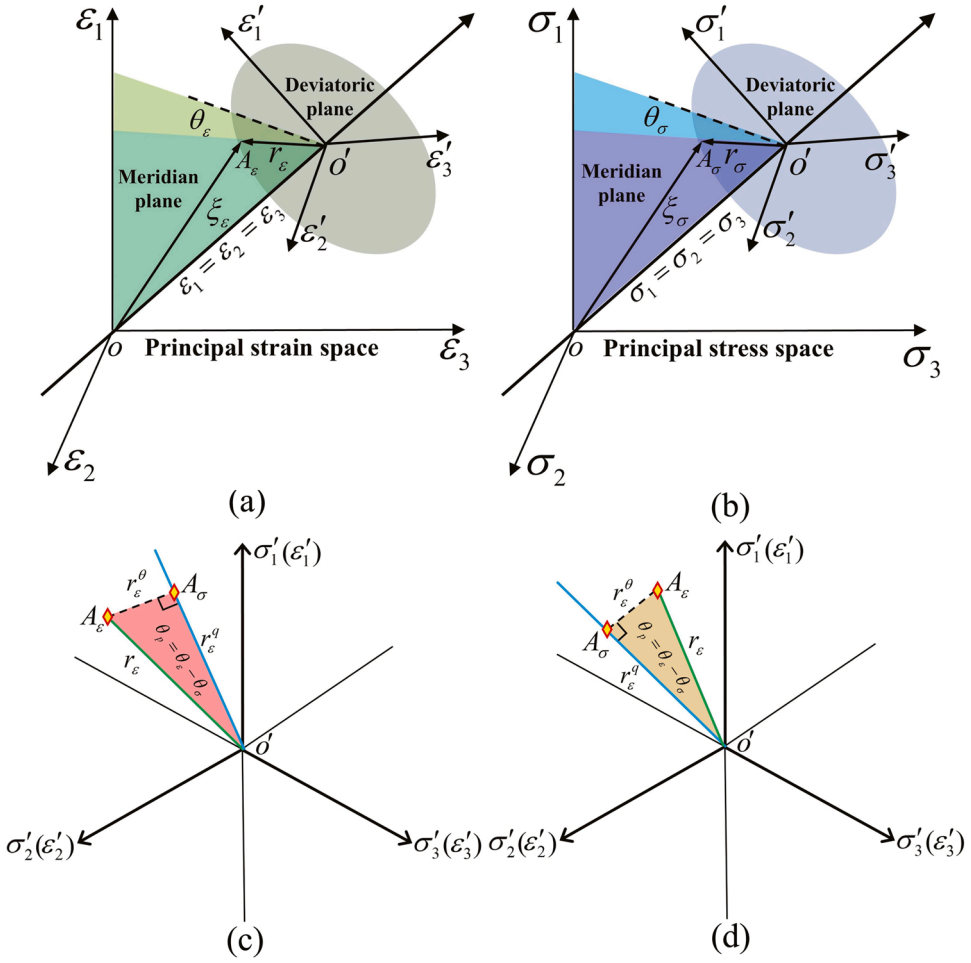

Fig. 2. Geometric presentation of principal strain and stress spaces. (a) Principal strain space; (b) Principal stress space; (c) Positive deflection Lode angle; (d) Negative deflection Lode angle. r^θ_σ is considered as the projection of the shear strain onto the direction perpendicular to the deviatoric stress, while r^q_σ is considered as the projection of the shear strain along the deviatoric stress direction.

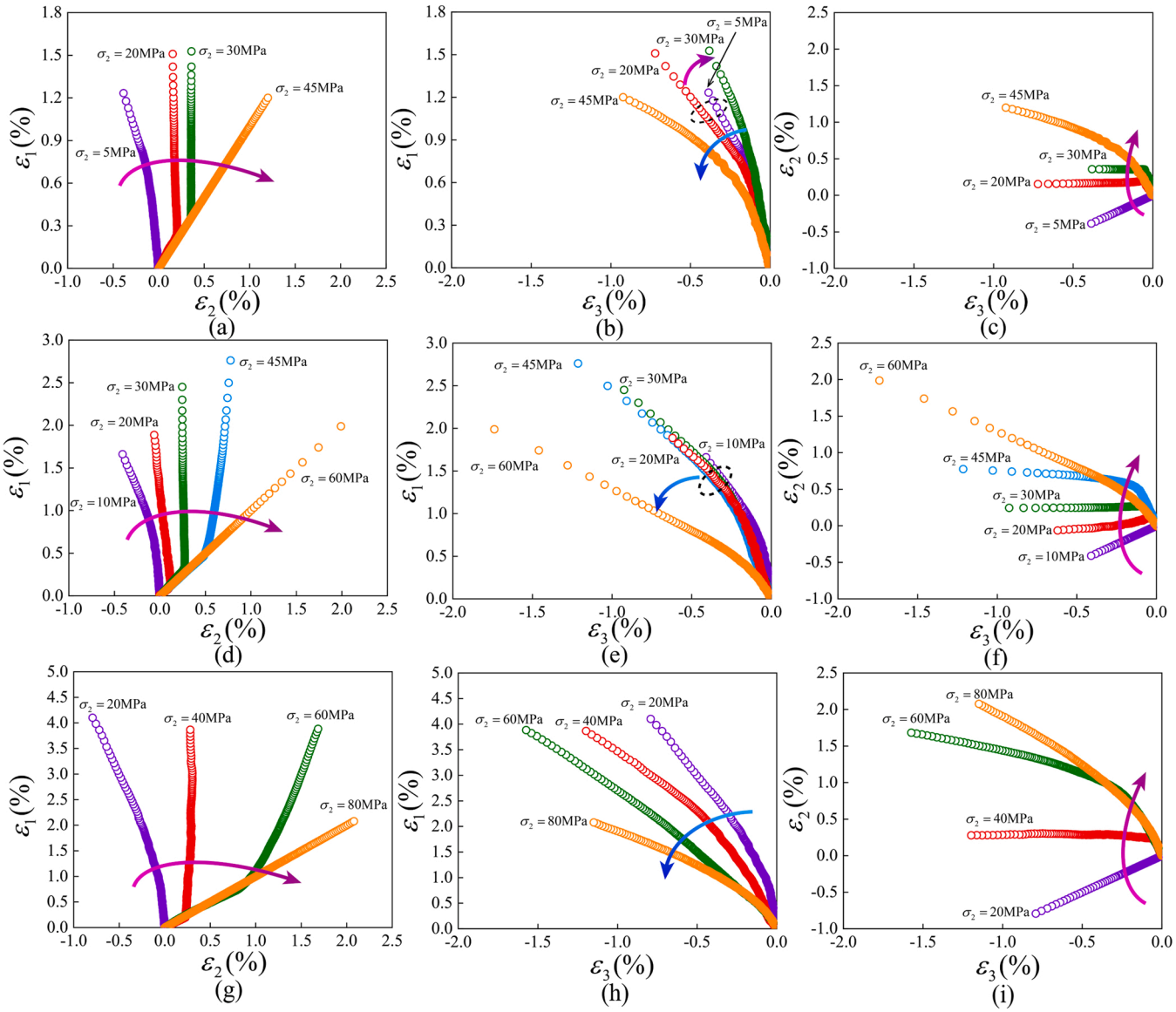

Fig. 3. Relationship between principal strains. (a), (b), and (c) are under σ_3 = 5MPa. (d), (e), and (f) are under σ_3 = 10MPa. (g), (h), and (i) are under σ_3 = 20MPa. The arrows are used to indicate the variation trend of strain path.

For stress state, the stress can be decomposed into hydrostatic pressure and deviatoric stress. The invariant ξ_σ is the length of OO', reflecting the extent of hydrostatic pressure. The invariant r_σ is the length of $A_\sigma O'$, reflecting the extent of deviatoric stress. The Lode angle for stress θ_σ is known as the angle between the vertical lines of ε'_2 axis and $A_\sigma O'$, as shown in Fig. 2b. θ_σ is equal to -30° under triaxial compression state ($\sigma_2 = \sigma_3$). θ_σ is equal to 30° under triaxial extension state ($\sigma_1 = \sigma_2$). Therefore, the stress state within the 3D principal stress space can be also identified by $(\xi_\sigma, r_\sigma, \theta_\sigma)$, given by [12]:

$$\left.\begin{aligned} \xi_\sigma &= \frac{I_1}{\sqrt{3}} \\ r_\sigma &= \sqrt{2J_2} \\ \theta_\sigma &= \frac{1}{3}\sin^{-1}\left(-\frac{3\sqrt{3}}{2}\frac{J_3}{J_2^{3/2}}\right) \end{aligned}\right\} \tag{3}$$

with

$$\left.\begin{aligned} I_1 &= \sigma_1 + \sigma_2 + \sigma_3 \\ I_2 &= \sigma_1\sigma_2 + \sigma_1\sigma_3 + \sigma_2\sigma_3 \\ I_3 &= \sigma_1\sigma_2\sigma_3 \\ J_2 &= \frac{[(\sigma_1-\sigma_2)^2 + (\sigma_1-\sigma_3)^2 + (\sigma_2-\sigma_3)^2]}{6} \\ J_3 &= \frac{2I_1^3 - 9I_1I_2 + 27I_3}{27} \end{aligned}\right\} \tag{4}$$

where σ_1 is maximum principal stress; σ_2 is intermediate principal stress; σ_3 is minimum principal stress. I_1 is the first invariant of the stress tensor, I_2 is the second invariant of the stress tensor, I_3 is the third invariant of the stress tensor, J_2 is the second invariant of the deviatoric stress tensor, J_3 is the third invariant of the deviatoric stress tensor.

3.2. Geometric presentation for LAD of deformation

In general, the stress path within deviatoric plane does not coincide with that for strain, as observed by several scholars [16,29]. The discrepancy between the Lode angles for stress and strain reflects the LAD of deformation [14], which characterizes the 3D anisotropic deformation characteristics of geotechnical materials. Theoretical studies indicate that LAD is crucial for accurately describing 3D deformation of geotechnical materials [14,30,31]. Therefore, quantitatively analyzing the LAD of deformation is crucial for understanding and describing the strain anisotropy of geotechnical materials. In this study, the concept of the deflection Lode angle (θ_p) under the common loading path is introduced to quantitatively analyze the LAD of deformation, defined as:

$$\theta_p = \theta_\varepsilon - \theta_\sigma \tag{5}$$

When θ_ε is larger than θ_σ, θ_p is positive, as depicted in Fig. 2c. When θ_ε is lower than θ_σ, θ_p is negative, as depicted in Fig. 2d. Based on the deflection Lode angle, the shear strain in the direction of Lode angle (r_σ^θ) and deviatoric stress (r_σ^q) can be introduced, as depicted in Fig. 2c and Fig. 2d, given by:

$$\left.\begin{aligned} r_\sigma^\theta &= \sin(\theta_p) r_\sigma \\ r_\sigma^q &= \cos(\theta_p) r_\sigma \end{aligned}\right\} \tag{6}$$

4. 3D deformation response of cement stone

4.1. Relationship between principal strains

The relationships between principal strains are discussed through the strain path within $\varepsilon_1 - \varepsilon_2$, $\varepsilon_1 - \varepsilon_3$, and $\varepsilon_2 - \varepsilon_3$ planes. In this study, the dilation is negative, while the contraction is positive. Under the same σ_3, with increasing σ_2, ε_2 shifts from dilation to contraction, which is also observed by other scholars [22]. This results in a clockwise rotation of the strain path within $\varepsilon_1 - \varepsilon_2$ and $\varepsilon_2 - \varepsilon_3$ planes, as depicted in Fig. 3. The stress paths at the ends correspond to triaxial compression and extension states, respectively. However, the extent of the clockwise rotation of the strain path within $\varepsilon_1 - \varepsilon_2$ and $\varepsilon_2 - \varepsilon_3$ planes varies slightly under different values of σ_3, which is closely related to the dilation and contraction characteristics of ε_2.

Under the condition of $\sigma_3 = 5$MPa, ε_2 under $\sigma_2 = 20$MPa and $\sigma_2 = 30$MPa remains approximately constant, which can be attributed to the balance of elastic strain (dilation) and plastic strain (contraction) [14]. Under the condition of $\sigma_3 = 10$MPa, ε_2 under $\sigma_2 = 20$MPa exhibits slight dilation, as the elastic strain (dilation) is more dominant than the plastic strain (contraction), while ε_2 under $\sigma_2 = 30$MPa is approximately constant. Besides, ε_2 under $\sigma_2 = 45$MPa exhibits contraction, which is owing to the fact that the plastic strain (contraction) is more dominant than the elastic strain (dilation). Under the condition of $\sigma_3 = 20$MPa, ε_2 under $\sigma_2 = 40$MPa is approximately constant, while ε_2 under $\sigma_2 = 60$MPa exhibits more significant contraction. The dilation and contraction characteristics of ε_2 are not only related to σ_2, but also to σ_3. It can be seen from Fig. 3 that a larger value of σ_2 leads to a more significant contraction of ε_2 by comparing the strain paths under the same σ_3, while a larger value of σ_3 results in a less significant contraction of ε_2 by comparing the strain paths under the same σ_2. With increasing σ_3, the corresponding value of σ_2 also increases. The trend of clockwise rotation of the strain path within $\varepsilon_1 - \varepsilon_2$ plane is becoming more significant, indicating a more significant contraction of ε_2. This suggests that the effect of σ_2 on the contraction of ε_2 is more significant than that of σ_3.

Under the same σ_3, with increasing σ_2, most of the strain paths within $\varepsilon_1 - \varepsilon_3$ plane exhibit a counterclockwise rotation. However, the variation in the strain path within $\varepsilon_1 - \varepsilon_3$ plane exhibits slight differences for different values of σ_3. Under the condition of $\sigma_3 = 5$MPa, the strain path under $\sigma_2 = 30$MPa appears to rotate clockwise, as depicted in Fig. 3b. Under the condition of $\sigma_3 = 10$MPa, the strain path under different values of σ_2 appears to overlap, as shown in Fig. 3e. Under the condition of $\sigma_3 = 20$MPa, the strain path appears to rotate significantly counterclockwise, as shown in Fig. 3h. With increasing σ_3, the trend of counterclockwise rotation of the strain path within $\varepsilon_1 - \varepsilon_3$ plane is becoming more significant, indicating a more significant dilation of ε_3, which is closely related to the frictional sliding of microcrack. The greater the frictional sliding of microcrack within $\sigma_1 - \sigma_3$ and $\sigma_2 - \sigma_3$ planes, the larger the resulting plastic minimum principal strain (dilation), as supported by reference [33]. With increasing σ_3, the corresponding value of σ_1 and σ_2 also increases. σ_1 and σ_2 promote the frictional sliding of microcrack within $\sigma_1 - \sigma_3$ and $\sigma_2 - \sigma_3$ planes, whereas σ_3 suppresses it [33]. Based on the above analyses, the effect of σ_1 and σ_2 on the dilation of ε_3 is more significant than that of σ_3.

4.2. Effect of intermediate principal stress on strain path

The strain paths within deviatoric and meridian planes are shown in Fig. 4. The strain path within meridian plane illustrates the correlation between volumetric deformation (ξ_ε) and shear deformation (r_ε). During the transition from stage II to stage III, the variation in 3D deformation response of cement stone is primarily attributed to the stress-induced anisotropy [16]. To distinguish between stage II and stage III, the strain path within meridian plane under true triaxial stress states is marked with a pentagram. From Fig. 4, it can be concluded that volumetric strain is more likely to develop during stage II, while shear strain predominates in stage III. This is primarily due to the fact that the development and friction sliding of fractures in the stage II are less pronounced compared to stage III [16,34,35]. When the cement stone is under elastic state, the strain path within meridian plane is represented as a straight line. As plastic deformation develops, the strain path within meridian plane transitions into a downward-surging curve, as shown in Fig. 4, which is consistent with previous study [16].

With increasing σ_2, the strain paths within meridian plane shift to the right and then to the left, as shown in Fig. 4. A similar phenomenon has also been observed by Liu et al. [16]. This behavior suggests that, when σ_2 is low, the volumetric strain tends to develop. However, when σ_2 is high, the shear strain is more likely to develop. Both hydrostatic pressure and Lode angle increase with increasing σ_2. Experimental results indicate that hydrostatic pressure promotes ductility, while Lode angle enhances brittleness [28]. The effect of hydrostatic pressure facilitates the generation of volumetric deformation, while the effect of Lode angle promotes shear deformation [16]. Therefore, when σ_2 is low, the effect of hydrostatic pressure dominates. When σ_2 is high, the effect of Lode angle dominates.

The strain path within deviatoric plane reflects the LAD of deformation [16,29]. The greater the deviation of the strain path from the reference line of θ_σ (RL), the higher the LAD of deformation [14]. During stage II, ε_1 is almost identical to ε_3, while σ_1 is identical to σ_3. As a result, θ_ε is approximately equal to $-30°$, while θ_σ is exactly $-30°$. Therefore, the strain path during Stage II exhibits negligible deviation from RL, as shown in Fig. 4. During stage III, both θ_ε and θ_σ decrease with increasing σ_1, subsequently exhibiting varying degrees in the LAD of deformation, as shown in Fig. 4. To distinguish between stage II and stage III, the strain path within deviatoric plane under true triaxial stress states is also marked with a pentagram. There is no deviation between the strain path under ($\theta_\sigma = -30°$, $\theta_\sigma = 30°$) and RL [16], as shown in Fig. 4. However, the strain path within deviatoric plane deviates from the RL under true triaxial stress state. Under the condition of $\sigma_3 = 5$MPa, θ_p is positive under $\sigma_2 = 20$MPa and negative under $\sigma_2 = 30$MPa. Under the condition of $\sigma_3 = 10$MPa, θ_p is also positive under $\sigma_2 = 20$MPa and negative

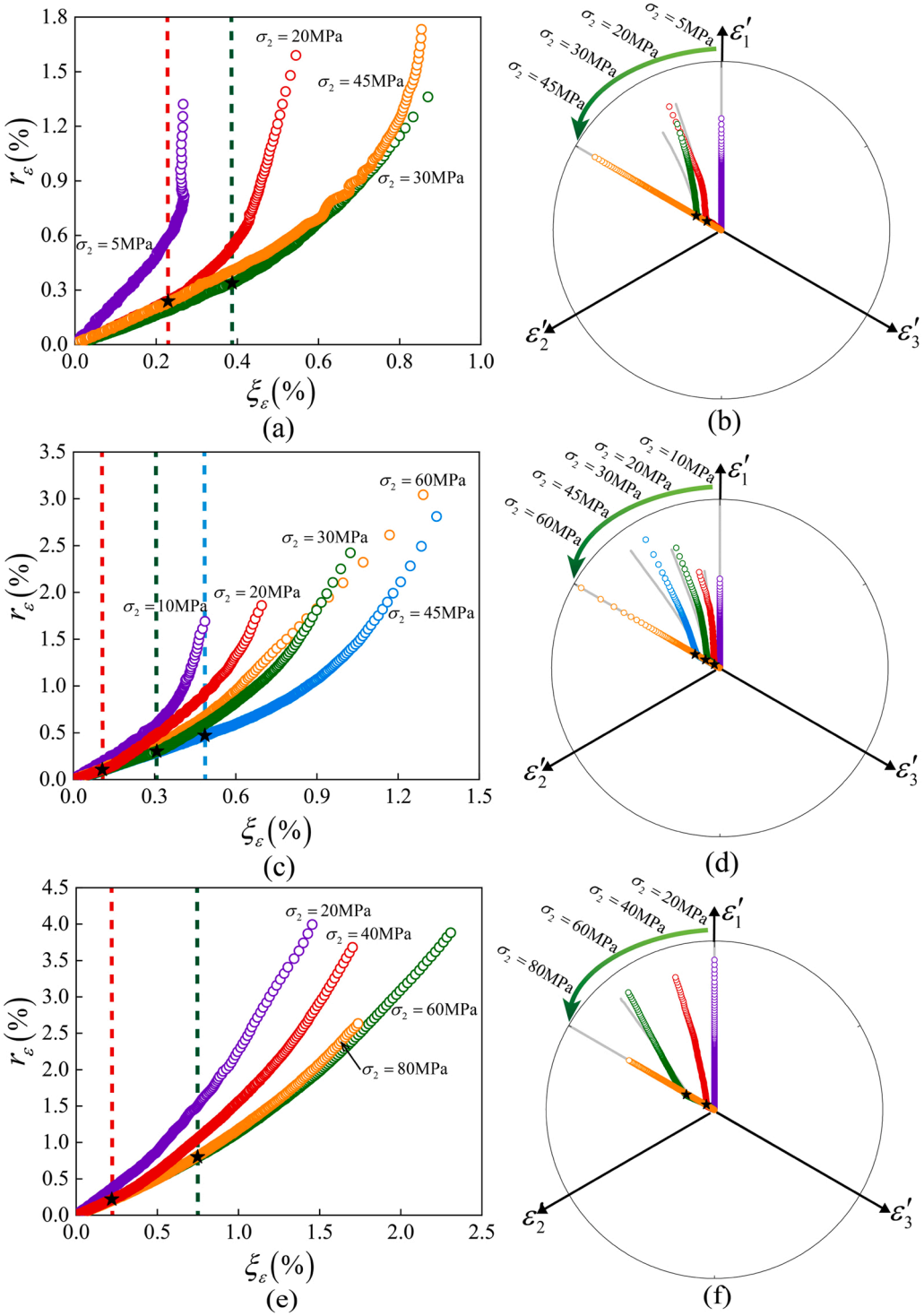

Fig. 4. Effect of intermediate principal stress on strain path. (a), (c), and (e) are strain path within meridian plane. (b), (d), and (f) are strain path within deviatoric plane. (a) and (b) are under σ_3 = 5MPa. (c) and (d) are under σ_3 = 10MPa. (e) and (f) are under σ_3 = 20MPa. The pentagram is the separation between stage II and stage III. The solid gray line is the RL, which can be determined by Eq. (6).

under $\sigma_2 = 30$MPa and $\sigma_2 = 45$MPa. Under the condition of $\sigma_3 = 20$MPa, θ_p is approximate zero under $\sigma_2 = 40$MPa and negative under $\sigma_2 = 60$MPa. Overall, θ_p transitions from positive to negative with the increasing σ_2, as depicted in Fig. 4.

As shown in Fig. 3, ε_3 is always dilation (negative), while ε_1 is always contraction (positive). ε_2 can either be dilation (negative) or contraction (positive). θ_p is jointly controlled by ε_1, ε_2, and ε_3. According to the definition of θ_p, ε_3 promotes θ_p as positive, while ε_1 promotes θ_p as negative. Positive ε_2 promotes θ_p as positive, while negative ε_2 promotes θ_p as negative. Besides, θ_p is also related to the stress state. Lode angle for stress is positively correlated to σ_2. The lower σ_2 (Lode angle for stress), the more pronounced the role of ε_3 in promoting θ_p as positive. Conversely, the higher σ_2 (Lode angle for stress), the more significant the role of ε_1 in promoting θ_p as negative. Therefore, the generation of a significant amount of plastic minimum principal strain (dilation) is the primary factor that leads to a positive value of θ_p, while the generation of

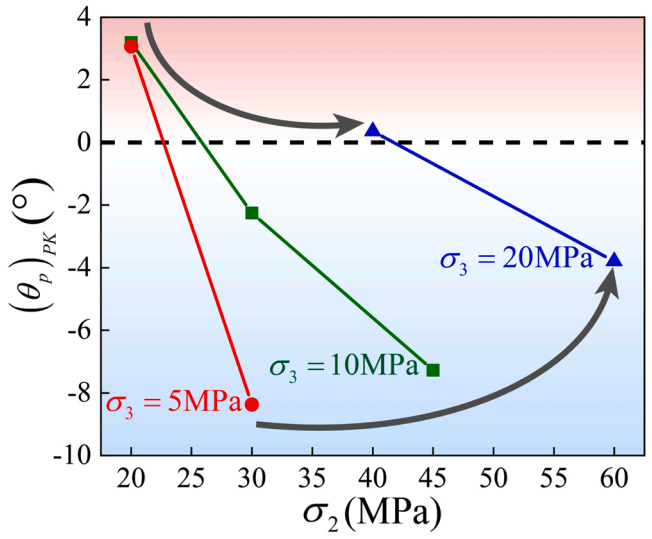

Fig. 5. LAD of deformation under various true triaxial stress states. The arrows are used to indicate the variation trend of $(\theta_p)_{PK}$ with increasing σ_3.

a significant amount of plastic maximum principal strain (contraction) is the primary factor responsible for a negative value of θ_p.

4.3. LAD of deformation

To quantitatively characterize the LAD of deformation, the deflection Lode angle at peak strength ($(\theta_p)_{PK}$) under various true triaxial stress states is depicted in Fig. 5. Under constant σ_3, $(\theta_p)_{PK}$ decreases with increasing σ_2, which is consistent with the observations of Liu et al. [16]. For the positive $(\theta_p)_{PK}$, dilatancy is the primary cause of LAD of deformation [29], and this effect is suppressed with increasing σ_3. For the negative $(\theta_p)_{PK}$, a notable feature is that the contraction of ε_2 significantly increases with increasing σ_3 and σ_2, as discussed in Section 4.1, directly leading to the decrease in LAD of deformation. This variation is related to the failure mode and the associated fractional sliding of microcracks. Under low value of σ_3, the localized failure mode typically manifests as shear bands within the $\sigma_1 - \sigma_3$ plane [24]. Therefore, the fractional sliding of microcracks primarily occurs within the $\sigma_1 - \sigma_3$ plane, which provides an explanation for the small variation in the ε_2 under low σ_3 conditions [36]. With increasing σ_3, the localized manner of failure is hindered by the high normal stress applied to the microcrack surfaces [16]. The failure mode gradually transitions from localized manner to delocalized manner, facilitating a substantial contraction of ε_2. Therefore, whether $(\theta_p)_{PK}$ is positive or negative, the Lode dependence of deformation decreases significantly with increasing σ_3, as indicated by the arrows in Fig. 5.

5. Conclusion

To investigate 3D deformation response of cement stone, a series of true triaxial compression tests were conducted with varying values of σ_2 and σ_3. Based on the principal strain space, the strains paths are analyzed within $\varepsilon_1 - \varepsilon_2$, $\varepsilon_1 - \varepsilon_3$, $\varepsilon_2 - \varepsilon_3$, meridian, and deviatoric planes. The key findings are summarized as follows.

1. With increasing σ_2, the strain paths within $\varepsilon_1 - \varepsilon_2$ and $\varepsilon_2 - \varepsilon_3$ planes rotate clockwise, which is closely related to the dilation and contraction characteristics of ε_2. With increasing σ_3 and σ_2, the trend of clockwise rotation of the strain path within $\varepsilon_1 - \varepsilon_2$ plane is becoming more significant, indicating a more significant contraction of ε_2.
2. With increasing σ_2, most of strain paths within $\varepsilon_1 - \varepsilon_3$ plane rotate counterclockwise. However, the strain paths within $\varepsilon_1 - \varepsilon_3$ plane under $\sigma_2 = 30$MPa and $\sigma_3 = 5$MPa appear to rotate clockwise. Under the condition of $\sigma_3 = 10$MPa, the strain paths within $\varepsilon_1 - \varepsilon_3$ plane under various values of σ_2 appear to overlap. This behavior is closely associated with the dilation of ε_3. With increasing σ_3 and σ_2, the trend of counterclockwise rotation of the strain path within $\varepsilon_1 - \varepsilon_3$ plane is becoming more significant, indicating a more significant dilation of ε_3.
3. The strain path within meridian plane directly reflects the relationship between volumetric strain and shear strain. The volumetric strain is more likely to develop during stage II, while shear strain predominates in stage III. This is primarily due to the fact that the development and friction sliding of fractures in the stage II are less pronounced compared to stage III. When σ_2 is low, the volumetric strain tends to develop with increasing σ_2. However, when σ_2 is high, the shear strain is more likely to develop with increasing σ_2.
4. The strain path within deviatoric plane directly reflects the LAD of deformation. θ_p is negatively correlated to σ_2. With increasing σ_2, θ_p transitions from positive to negative. Whether θ_p is positive or negative, the Lode dependence of deformation decreases significantly with increasing σ_3. For positive θ_p, this phenomenon is related to dilatancy of cement stone, which is suppressed with increasing σ_3. For negative θ_p, this phenomenon is related to the failure mode and the associated fractional sliding of microcracks. The failure mode gradually transitions from localized manner to delocalized manner, facilitating a substantial contraction of ε_2.

CRediT authorship contribution statement

Ying Xu: Writing – original draft, Investigation, Data curation. **Dongping Liu:** Investigation, Data curation. **Bangbiao Wu:** Writing – review & editing, Visualization. **Jiacun Liu:** Writing – review & editing, Methodology, Conceptualization.

Declaration of Competing Interest

The authors declare that they have no known competing financial interests or personal relationships that could have appeared to influence the work reported in this paper.

Acknowledgements

This work has been sponsored by the National Natural Science Foundation of China under Grants #42141010.

Appendix. stress-strain curve of cement stone

The stress-strain of cement stone under various true triaxial stress states is shown in Fig. 6. It is worth noting that the cement stone consistently exhibits volumetric contraction.

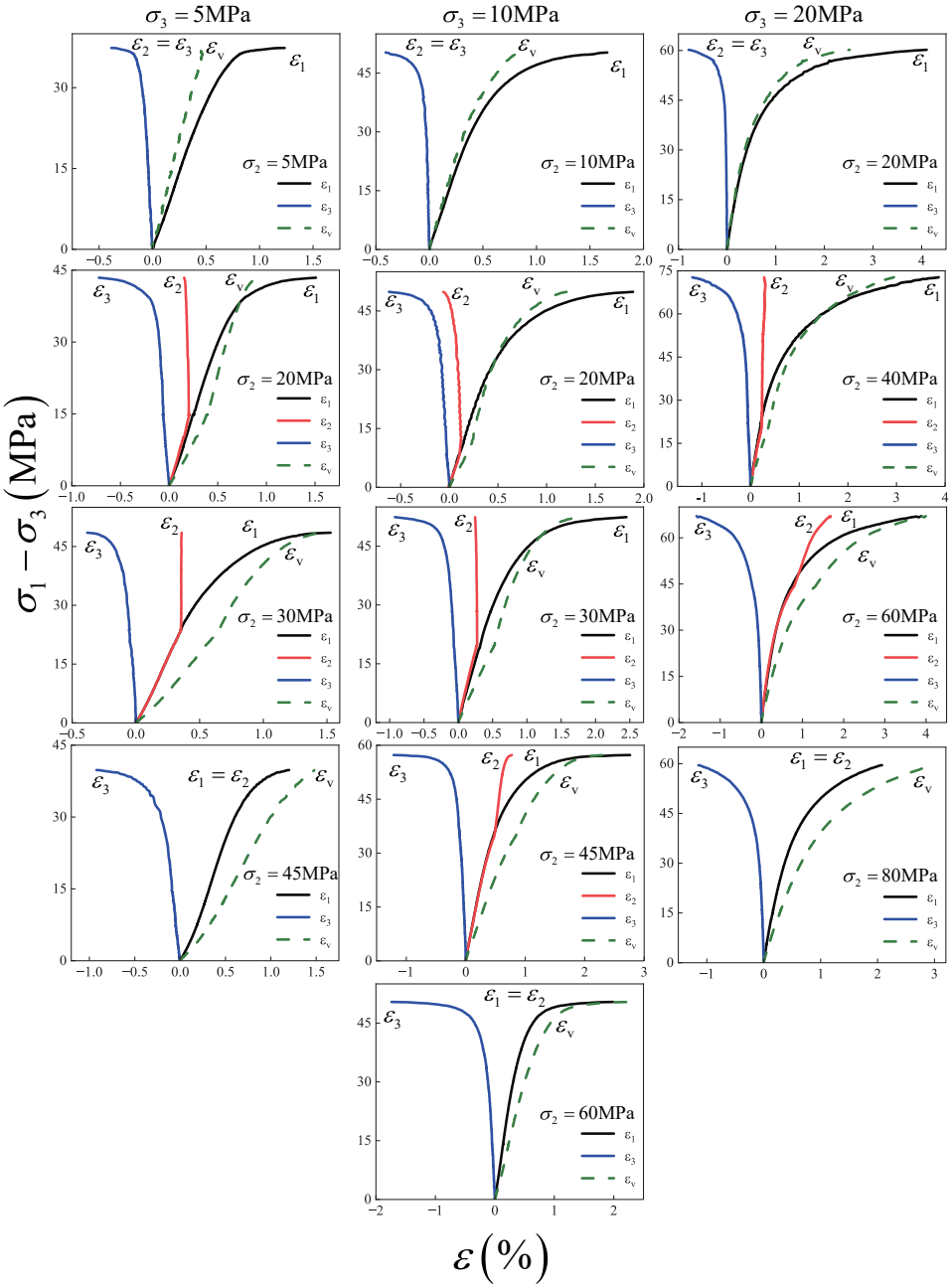

Fig. 6. Stress-strain curve of cement stone

References

[1] J. Liu, X. Li, J. Xiao, Y. Xie, K. Xia, Three-dimensional strength criterion for rocks: a review, Energy Rev. 3 (4) (2024) 100102.

[2] K. Xia, M. Wang, Y. Fu, B. Wu, Y. Xu, W. Yao, Advances in dynamic test of deep rocks considering in-situ mechanical and hydraulic conditions, Deep Resour. Eng. 1 (2) (2024) 100020.

[3] X.-T. Feng, C.-X. Yang, B.-G. He, Z.-B. Yao, L. Hu, W. Zhang, R. Kong, J. Zhao, Z.-B. Liu, X. Bi, Artificial intelligence technology in rock mechanics and rock engineering, Deep Resour. Eng. 1 (2) (2024) 100008.

[4] H. Yang, L. Wang, C. Yang, J. Zhao, G. Huang, Y. Guo, W.V. Liu, Mechanical performance of oil-well cement slurries cured and tested under high-temperatures and high-pressures for deep-well applications, Cem. Concr. Res. 175 (2024) 107355.

[5] J. Liu, X. Wu, Z. Li, W. Song, Y. Liu, Q. Shi, R. Chen, Mechanical properties and nonlinear deformation description model of cement stone, Geoenergy Sci. Eng. 223 (2023) 211578.

[6] F. Xu, Z. Xu, S. Tang, Q. Ren, Y. Guo, L. Wang, Z. Hou, Z. Liu, Evolution of physical and mechanical properties of cementing materials during underground energy exploitation and storage, J. Energy Storage 45 (2022) 103775.

[7] S. Zhou, R. Liu, H. Zeng, Y. Zeng, L. Zhang, J. Zhang, X. Li, Mechanical characteristics of well cement under cyclic loading and its influence on the integrity of shale gas wellbores, Fuel 250 (2019) 132–143.

[8] Y. Yang, Y. Deng, Mechanical properties of hybrid short fibers reinforced oil well cement by polyester fiber and calcium carbonate whisker, Constr. Build. Mater. 182 (2018) 258–272.

[9] Y. Xu, J. Xiao, J. Liu, K. Xia, True-triaxial strength characteristics of cement stone subjected to sulfuric acid corrosion: an experimental and theoretical study, Constr. Build. Mater. 444 (2024) 137877.

[10] J. Liu, X. Li, Y. Xu, K. Xia, A three-dimensional nonlinear strength criterion for rocks considering both brittle and ductile domains, Rock. Mech. Rock. Eng. 57 (2024) 5863–5881.

[11] J. Liu, J. Xiao, X. Li, Z. Cao, Y. Xu, A Novel Mohr–Coulomb–Matsuoka–Nakai strength criterion for rocks considering brittle–ductile domain, Rock. Mech. Rock. Eng. 57 (2024) 11033–11048.

[12] J. Xiao, J. Liu, Y. Xu, X. Li, A. Liu, K. Xia, An improved three-dimensional extension of Hoek–Brown criterion for rocks, Geomech. Geophys Geo-Energy Geo-Resour. 10 (1) (2024) 129.
[13] J. Wang, S. Wu, X. Chang, H. Cheng, Z. Zhou, Z. Ren, A novel three-dimensional nonlinear unified failure criterion for rock materials, Acta Geotech. 19 (2024) 3337–3375.
[14] J. Liu, X. Li, C. Wang, Y. Xu, K. Xia, A three-dimensional elastoplastic constitutive model incorporating Lode angle dependence, Geomech. Energy Environ. 38 (2024) 100567.
[15] M. Li, J. Lu, H. Xie, M. Gao, H. Gao, D. Shang, C. Jiang, Nonlinear mechanical and 3D rupture morphology of saturated porous sandstone under true triaxial stress, Rock. Mech. Rock. Eng. 57 (2024) 6837–6859.
[16] J. Liu, W. Jia, H. Duan, X. Li, K. Xia, Experimental study on the deformation and failure characteristics of cement stone under true triaxial stress state, Constr. Build. Mater. 449 (2024) 138397.
[17] X. Ma, B.C. Haimson, Failure characteristics of two porous sandstones subjected to true triaxial stresses, J. Geophys. Res. Solid Earth 121 (9) (2016) 6477–6498.
[18] X. Ma, M.D. Ingraham, On the applicability of Nadai and Mogi failure criteria to porous sandstones, Rock. Mech. Rock. Eng. 51 (12) (2018) 3835–3843.
[19] S. Wu, S. Zhang, G. Zhang, Three-dimensional strength estimation of intact rocks using a modified Hoek-Brown criterion based on a new deviatoric function, Int. J. Rock. Mech. Min. Sci. 107 (2018) 181–190.
[20] J. Wang, S. Wu, H. Cheng, J. Sun, X. Wang, Y. Shen, A generalized nonlinear three-dimensional Hoek–Brown failure criterion, J. Rock. Mech. Geotech. Eng. 16 (8) (2024) 3149–3164.
[21] Z. Song, G. Yin, P.G. Ranjith, M. Li, J. Huang, C. Liu, Influence of the intermediate principal stress on sandstone failure, Rock. Mech. Rock. Eng. 52 (9) (2019) 3033–3046.
[22] S. Zhang, S. Wu, G. Zhang, Strength and deformability of a low-porosity sandstone under true triaxial compression conditions, Int. J. Rock. Mech. Min. Sci. 127 (2020) 104204.
[23] R. Kong, X.-T. Feng, X. Zhang, C. Yang, Study on crack initiation and damage stress in sandstone under true triaxial compression, Int. J. Rock. Mech. Min. Sci. 106 (2018) 117–123.
[24] Z. Cao, J. Liu, J. Xiao, J. Zhang, Y. Xu, Strength characteristics and energy evolution of cement stone under true-triaxial loading conditions, Constr. Build. Mater. 432 (2024) 136690.
[25] J. Lu, G. Huang, H. Gao, X. Li, D. Zhang, G. Yin, Mechanical properties of layered composite coal-rock subjected to true triaxial stress, Rock. Mech. Rock. Eng. 53 (9) (2020) 4117–4138.
[26] J. Lu, G. Yin, D. Zhang, H. Gao, C. Li, M. Li, True triaxial strength and failure characteristics of cubic coal and sandstone under different loading paths, Int. J. Rock. Mech. Min. Sci. 135 (2020) 104439.
[27] H. Xie, J. Lu, C. Li, M. Li, M. Gao, Experimental study on the mechanical and failure behaviors of deep rock subjected to true triaxial stress: a review, Int. J. Min. Sci. Technol. 32 (5) (2022) 915–950.
[28] C. Couture, P. Besuelle, A true triaxial experimental study on porous Vosges sandstone: from strain localization precursors to failure using full-field measurements, Int. J. Rock. Mech. Min. Sci. 153 (2022) 105031.
[29] Z. Song, Z. Zhang, P.G. Ranjith, W. Zhao, C. Liu, Experimental study on the influence of hydrostatic stress on the Lode angle effect of porous rock, Int. J. Min. Sci. Technol. 32 (4) (2022) 727–735.
[30] J. Liu, Y. Xu, J. Xiao, C. Wang, K. Xia, Three-dimensional elastoplastic constitutive model for cement stone based on fractional flow rule, Geomech. Geophys. Geo-Energy Geo-Resour. 10 (1) (2024) 191.
[31] J. Liu, X. Li, C. Wang, Y. Xu, K. Xia, Fractional elastoplastic constitutive model for sandstone subjected to true-triaxial compressive loading, J. Rock. Mech. Geotech. Eng. 17 (9) (2025) 5683–5694.
[32] X.-T. Feng, B. Haimson, X. Li, C. Chang, X. Ma, X. Zhang, M. Ingraham, K. Suzuki, ISRM suggested method: determining deformation and failure characteristics of rocks subjected to true triaxial compression, Rock. Mech. Rock. Eng. 52 (6) (2019) 2011–2020.
[33] X. Zhou, Q. Ha, Y. Zhang, K. Zhu, Analysis of deformation localization and the complete stress–strain relation for brittle rock subjected to dynamic compressive loads, Int. J. Rock. Mech. Min. Sci. 41 (2) (2004) 311–319.
[34] L.-Y. Zhao, Q.-Z. Zhu, J.-F. Shao, A micro-mechanics based plastic damage model for quasi-brittle materials under a large range of compressive stress, Int. J. Plast. 100 (2018) 156–176.
[35] Q.Z. Zhu, D. Kondo, J.F. Shao, Micromechanical analysis of coupling between anisotropic damage and friction in quasi brittle materials: Role of the homogenization scheme, Int. J. Solids Struct. 45 (5) (2008) 1385–1405.
[36] F. Meng, Z. Yue, M. Li, J. Han, Q. Cai, W. Wang, D. Hu, C. Zhang, Frictional sliding behaviour of rough fracture in granite under true triaxial loading with implications for fault reactivation, Rock. Mech. Rock. Eng. 57 (1) (2024) 197–217.

Prof. Ying Xu is currently an associate professor and a doctoral supervisor in School of civil engineering at Tianjin University. Her research involved dynamical catastrophic mechanisms in ice-rock avalanche hazards, deep earth CO_2 sequestration, and environmental rock dynamics. Over the past five years, she has led three National Natural Science Foundation of China (NSFC) projects and published approximately 50 scholarly articles.